

**SURFACTANT CONCENTRATION AND END EFFECTS  
ON FOAM FLOW IN POROUS MEDIA**

**SUPRI TR — 120 Report**

**By  
Osman G. Apaydin  
Anthony R. Kavscek**

**October 2000**

**Work Performed Under Contract No. DE-FC26-00BC15311**

**Prepared for  
U.S. Department of Energy  
Assistant Secretary for Fossil Energy**

**Thomas Reid, Project Manager  
National Petroleum Technology Office  
P.O. Box 3628  
Tulsa, OK 74101**



## Table of Contents

	<u>Page</u>
List of Tables	iii
List of Figures	iii
Acknowledgements	v
Abstract	vi
1. Introduction	1
1.1 Gas Mobility Reduction	2
1.2 Modeling Foam Displacement	5
2. Experimental Setup and Procedures	8
3. Experimental Summary	12
4. Transient Displacements	15
4.1 Foam Texture	17
4.2 Aqueous Phase Saturation	18
4.3 Pressure Drop	20
5. End Effect	21
6. Conclusion	24
Nomenclature	26
References	28

## List of Tables

	<u>Page</u>
1. Parameter values.	33
2. Limiting capillary pressure and surface tension values [ $\sigma$ from Bertin <i>et al.</i> (1999)].	33

## List of Figures

	<u>Page</u>
1. Cumulative water recovery.	34
2. Water saturation in cross sections along the length of the sandpack. Below each image the position of the cross section is given (a) 1 wt% case at 0.52 PVI; (b) 0.1 wt% case at 0.51 PVI; (c) 0.01 wt% case at 0.51 PVI; (d) 0.005 wt% case at 0.55 PVI.	35,36
3. Steady state aqueous-phase saturation profiles.	37
4. Experimental transient pressure profiles, 1 wt% case.	38
5. Model transient flowing bubble texture profiles (a) 1 wt% case; (b) 0.1 wt% case; (c) 0.02 wt% case; (d) 0.01 wt% case; (e) 0.005 wt% case.	39
6. Experimental (symbols connected by dashed lines) and model (solid lines) transient aqueous-phase saturation profiles. (a) 1 wt% case; (b) 0.1 wt% case; (c) 0.02 wt% case; (d) 0.01 wt% case; (e) 0.005 wt% case.	40
7. Experimental (symbols connected by dashed lines) and model (solid lines) transient pressure profiles. (a) 1 wt% case; (b) 0.1 wt% case; (c) 0.02 wt% case; (d) 0.01 wt% case; (e) 0.005 wt% case.	41
8. Flowing foam fraction profiles based upon a local equilibrium assumption,	

wt% case.	42
9. Flowing foam fraction profiles based upon a local equilibrium assumption, 0.1 wt% case.	43

## **Acknowledgements**

This work was supported by the Assistant Secretary for Fossil Energy, Office of Oil Gas and Shale Technologies of the U.S. Department of Energy under Contract No. DE-FG22-96BC14994 to Stanford University. Likewise, the support of the SUPRI-A Industrial Affiliates is acknowledged.

Acknowledgement is made to the donors of The Petroleum Research Fund, administered by the ACS, for partial support of this research.

## **Abstract**

Foaming injected gas is a useful and promising technique for achieving mobility control in porous media. Typically, such foams are aqueous. In the presence of foam, gas and liquid flow behavior is determined by bubble size or foam texture. The thin-liquid films that separate foam into bubbles must be relatively stable for a foam to be finely textured and thereby be effective as a displacing or blocking agent. Film stability is a strong function of surfactant concentration and type. This work studies foam flow behavior at a variety of surfactant concentrations using experiments and a numerical model. Thus, the foam behavior examined spans from strong to weak.

Specifically, a suite of foam displacements over a range of surfactant concentrations in a roughly  $7 \mu\text{m}^2$ , one-dimensional sandpack are monitored using X-ray computed tomography (CT). Sequential pressure taps are employed to measure flow resistance. Nitrogen is the gas and an alpha olefin sulfonate (AOS 1416) in brine is the foamer. Surfactant concentrations studied vary from 0.005 to 1 wt%. Because foam mobility depends strongly upon its texture, a bubble population balance model is both useful and necessary to describe the experimental results thoroughly and self consistently. Excellent agreement is found between experiment and theory.



## 1. Introduction

Foam is suggested by many investigators to improve the sweep efficiency of multi-phase displacement processes. Aqueous foams are most common and are formed by dispersing non-wetting gases within a continuous surfactant-laden liquid phase either by alternating or co-injection of gas and surfactant solution into porous media. For example, surfactant soil flushing is recommended for aquifer remediation of dense organic liquids (Wunderlich *et al.* 1992). However, flushing low permeability regions and depressions in the aquifer where the dense organic phase might accumulate is difficult. Injecting gas with the surfactant solution to generate a foam in situ enhances sweep and improves remediation (Hirasaki *et al.* 1997a; 1997b).

In enhanced oil recovery (EOR) gases such as steam, carbon dioxide, enriched hydrocarbons, and nitrogen are injected into oil reservoirs to improve recovery. These gases are usually less viscous than water, and oil and they often channel selectively through high permeability zones or rise to the top of the reservoir by gravity segregation. As a result, sweep efficiency decreases and the amount of oil left behind increases. Again, foaming the gas might overcome the mobility problem of gas-drive fluids and improve the contact with the oil because foam encounters large flow resistance in porous media (c.f., Hoefner *et al.* 1994; Aarra *et al.* 1996; Patzek 1996).

Despite the varied field applications, foam behavior in porous media is far from understood. This work probes experimentally the effect of surfactant concentration on foam flow in homogeneous porous media and demonstrates a model to predict accurately the generation, coalescence, and transport of foam. To this end, experiments in a homogeneous sand with a commercial surfactant at a variety of surfactant concentrations have been conducted. We hope to provide a description of foam that begins to address the variable surfactant concentration conditions.

The progress of foam displacement at low injection rates is monitored with X-ray computed tomography (CT) and measurement of pressure profiles. Some experiments exhibit end effects that are well described by application of the model under local equilibrium conditions. Even at low surfactant concentrations, a significant effect of foam on displacement efficiency is witnessed.

Interaction of foam with oil is not included here to avoid confusing foam-oil effects with foam coalescence. However, foam-oil interactions are discussed elsewhere including their incorporation into a mechanistic simulation framework (Bergeron *et al.* 1993; Myers and Radke 1999). Likewise, experiments regarding foam generation and propagation in multidimensional heterogeneous porous media have also been conducted (Bertin *et al.* 1999). Before discussing the experimental setup, results, simulation of the experiments, and the interpretation of end effects in foam flow, it is helpful to review gas-mobility reduction mechanisms and the role of surfactant in foam displacement.

### **1.1 Gas Mobility Reduction**

Foam reduces gas mobility dramatically. For instance, Persoff *et al.* (1991) report dimensionless foam flow resistance factors (flow resistance multiplied by the ratio of permeability upon liquid-phase viscosity) up to 200 for steady-state foam flow in  $1.3 \mu\text{m}^2$  Boise sandstone. The first mechanism by which gas alters foam mobility is associated with moving bubbles and rearrangement of bubble interfacial area. Recall that a lamella is a thin-liquid film that separates bubbles. Foam bubbles in porous media are as large or larger than characteristic pore size; thus, bubbles and lamellae completely span pores (Hirasaki and Lawson 1985; Ettinger and Radke 1992). This foam configuration is referred to as a confined foam because of the constraining effect of the porous medium on foam structure (Kovscek and Radke 1994).

Confined gas bubbles transport by sliding over lubricating liquid films that coat pore walls (Bretherton 1961) and liquid-filled pore corners (Wong *et al.* 1995a; 1995b). At low bubble velocities (*i.e.*, capillary number) characteristic of flow in porous media, the pressure drop to drive a bubble at a constant velocity exceeds that of an equivalent volume of liquid, thereby increasing the effective viscosity of the gas phase. Additionally, surfactant movement from the front of a moving bubble to the rear induces a surface-tension gradient that slows bubble motion and so increases the effective viscosity (Hirasaki and Lawson 1985).

The second mechanism that reduces gas mobility is trapping of the gas phase. The fraction of gas that is stationary in a foam is quantifiable using gas-phase tracers (Gillis and Radke 1990; Friedmann *et al.* 1991). Experimental measurements of trapped gas in sandstone containing foam place the fraction of gas that is not flowing between 0.85 and 0.99. The most important factors governing bubble trapping include pressure gradient, pore geometry, and foam texture; however, the dependence of trapped fraction on these factors is not established. Gillis and Radke (1990) find no consistent trend of trapped fraction with varying liquid or gas velocity, while Friedmann *et al.* (1991) find that the fraction of trapped gas increases slightly with gas velocity at a constant gas fractional flow. Hanssen (1993a) shows experimentally that high permeability (say  $30 \mu\text{m}^2$ ) reduces the tendency of foam to trap and remain stationary.

On the pore level, gas flowing in the form of a foam tends to flow through the high permeability and high porosity zones. The wetting phase occupies the smallest pore channels. Thus, trapping of gas occurs in the intermediate sized pores (Kovscek and Radke 1994). Apparently, capillary forces are sufficient to immobilize a large fraction of foam bubbles (Rossen and Gauglitz 1990; Hanssen 1993b; Cohen *et al.* 1997; Kharabaf and Yortsos 1998). Hence, pore space is blocked that would otherwise carry gas and gas relative permeability is reduced significantly.

These mobility reduction mechanisms require multiple disconnected bubbles and stable thin-liquid films between bubbles. Film stability is provided by surfactant molecules that array themselves near gas-liquid interfaces where the identically charged interfaces repel each other.

Foam films are meta-stable as opposed to thermodynamically stable. The surfactant induced stabilizing forces are sensitive to surfactant concentration, surfactant structure, and to ionic strength of the aqueous solution. Other sources elaborate on the origin and behavior of stabilizing forces in foam films (Vrij 1966; Jiménez and Radke 1989; Chambers and Radke 1991; Hirasaki 1991; Bergeron and Radke 1992).

Khatib *et al.* (1988) first suggested that foam-film strength was directly related to gas mobility reduction in the presence of foam. For a given surfactant and concentration, they observed dramatic foam coarsening at a particular capillary pressure that they termed the "limiting capillary pressure",  $P_c^*$ . Above  $P_c^*$ , foam films are unstable, coalescence of foam lamellae is significant, and high gas mobility emerges. Below  $P_c^*$ , coalescence is significantly less and gas mobility is low. To further connect foam film stability and gas mobility, the rupture capillary pressure of single foam films was measured at a variety of surfactant and brine concentrations and either compared with the steady-state pressure drops of  $N_2$  foam in oil-free beadpacks (Aronson *et al.* 1994). Stable, low mobility foam with large  $P_c^*$  was generated once the rupture pressure of individual foam films exceeded the medium capillary pressure. Reviews of transport, generation, and coalescence of foam bubbles are given elsewhere (Chambers and Radke 1991; Kavscek and Radke 1994; Rossen 1995).

## 1.2 Modeling Foam Displacement

A quantitative model is necessary to interpret the experimental results to follow. The mechanisms of gas mobility reduction by foam derive from the flow resistance of discrete bubbles, as discussed in the previous section. Thus, it seems natural to compute directly gas mobility from the texture or number concentration of bubbles inside porous media. A balance that tracks the evolution of the number concentration of bubbles is one means to link bubbles and gas mobility. Foam is treated mathematically as a nonreactive, time-dependent component of the gas phase. Previous work has formulated a population balance approach that is mechanistic in that well documented foam mechanisms are incorporated into a continuum balance equation for foam (Kovscek *et al.* 1995; Kovscek *et al.* 1997). The theory reproduces well experimental foam behavior at surfactant concentrations around 1 wt%. However, this approach has not been tested over a variety of surfactant concentrations and especially at low concentration where foam is weak.

In addition to the requisite material balances for water, surfactant, and nitrogen chemical species, a transient balance on the mean bubble size is written. In one dimension (Kovscek *et al.* 1995):

$$\frac{\partial}{\partial t} \left[ \phi (S_f n_f + S_t n_t) \right] + \frac{\partial}{\partial x} (u_f n_f) = \phi S_g \left[ k_1 v_w v_f^{1/3} - k_{-1} v_f n_f \right] + Q_b \quad (1)$$

where  $t$  denotes time,  $\phi$  is porosity,  $S$  is saturation,  $n$  is bubble concentration (bubbles per unit volume of gas),  $u$  is Darcy velocity,  $v$  is the interstitial velocity ( $v = u / S\phi$ ),  $k_1$  is the generation rate constant,  $k_{-1}$  is the coalescence rate constant, and  $Q_b$  is a source/sink term for bubbles. The subscript f refers to flowing foam, t to trapped foam, g to the gas phase, and w to the aqueous phase. Units of the various terms are listed in Table 1. We refer to number concentration, foam texture, and bubble texture synonymously throughout this work.

Note the similarity of Eq. (1) with the usual mass and energy balances for transport processes in porous media. The first term on the left of Eq. (1) is the accumulation of foam bubbles and the second term is the flux of foam bubbles. The first term on the right of Eq. (1) represents the net generation of foam bubbles, i.e., generation minus coalescence. Foam generation is taken as a power-law expression that is proportional to the interstitial liquid velocity multiplied by the 1/3 power of the gas velocity. The origin of these velocity dependencies for generation may be found elsewhere (Kovscek and Radke 1996).

Foam coalesces when bubbles flow into so-called termination sites (Jiménez and Radke 1989; Kovscek and Radke 1994). Hence, foam coalescence is taken as proportional to the interstitial flux of foam,  $v_f n_f$ . The coalescence rate constant varies strongly with the local capillary pressure, surfactant formulation, and aqueous-phase concentration. A high rate of coalescence is expected at low surfactant concentration because there is little surfactant to exert a stabilizing effect. A dramatically lower rate is expected when the concentration is high and the surfactant is known to produce stable foam, provided that the porous medium does not exceed limiting capillary pressure.

The effects of surfactant concentration and capillary pressure are embodied in the coalescence rate constant. The following functional relationship is employed:

$$k_{-1} = k_{-1}^o \left( \frac{P_c}{P_c^* - P_c} \right)^2 \quad (2)$$

where  $k_{-1}^o$  is a scaling factor that is set constant and  $P_c^*$  is the limiting capillary pressure discussed earlier in Section 1.1,  $k_{-1}$  becomes very large as  $P_c$  and  $P_c^*$  approach equality. The major task of this work is to infer the functional form of  $P_c^*$  with respect to surfactant concentration from laboratory experiments and to simulate these experiments quantitatively.

To solve Eq. (1), additional information on the convection of foam and wetting aqueous phase is required. Darcy's law is retained including the formalism of multiphase relative permeability curves. For the gas phase, we replace viscosity with an effective viscosity relation for foam:

$$\mu_f = \mu_g + \frac{\alpha n_f}{v_f^{1/3}} \quad (3)$$

where  $\alpha$  is a constant of proportionality. This expression follows directly from theoretical studies of bubble flow in capillary tubes and porous media (Bretherton 1961; Hirasaki and Lawson 1985; Wong *et al.* 1995a,b).

Foam also reduces gas mobility by reducing the gas-phase relative permeability. Since the portion of gas that actually flows partitions into the largest pores with the least flow resistance, we employ a so-called ‘‘Stone-type’’ relative permeability model (Stone 1970), although the ideas employed here predate Stone (Saraf and Fatt 1967). Hence, the relative permeability of the flowing foam is only a function of  $S_f$ . Because the wetting phase partitions selectively to the smallest pore space, the aqueous-phase relative permeability is unaffected by flowing and stationary foam. This statement is well established by experiment (Bernard *et al.* 1965; Holm 1968; Sanchez *et al.* 1986; Huh and Handy 1989; De Vries and Wit 1990). Aqueous phase relative permeability remains solely a function of  $S_w$ . Clearly, the relative permeability of the stationary foam is zero. A standard exponent relative permeability model is used

$$k_{rw} = k_{rw}^o S_{wd}^a \quad (4a)$$

$$k_{rf} = k_{rg}^o S_{fd}^b \quad (4b)$$

with  $a$  and  $b$  representing the exponents for water and gas flow, respectively. The superscript  $o$  indicates the endpoint relative permeability. The reduced saturations,  $S_{id}$ , are written

$$S_{fd} = X_f(1 - S_{wd}) \quad (5a)$$

$$S_{wd} = \frac{(S_w - S_{wir})}{(1 - S_{wir})} \quad (5b)$$

where  $X_f = S_f/S_g$  is the fraction of the gas phase that is flowing and  $S_{wir}$  is the irreducible aqueous-phase saturation. The relative permeability exponents and endpoint relative permeabilities represent values for non-dispersed, continuum gas-liquid flow in the porous medium.

## 2. Experimental Setup and Procedures

The experimental program was designed to obtain an understanding of how overall recovery, pressure-drop profiles, and water saturation profiles shift with changing surfactant concentration. For this purpose, we report 5 foam flow experiments using two different sand packs.

The apparatus consists of a 0.51 m (20 in) long aluminum sandpack with a 0.051 m (2 in) inner diameter. It was packed with dry 100-120 mesh Ottawa sand in an upright position and pneumatic vibrators were used to ensure good settling. Screens at the inlet and outlet faces of the sandpack prevented washout of sand grains. The average porosity and permeability of pack 1 are 35% and  $6.7 \mu\text{m}^2$ , whereas for pack 2 the values are 36% and  $7.0 \mu\text{m}^2$ . CT images, as described later, confirmed that the packs were homogeneous. Permeability values reported are permeability to brine.

The sandpack attaches to an L-shaped mounting bracket for bolting of the apparatus to a precision positioning system (Compumotor, RP240, Parker Hannifin

Corp.). Displacements were conducted with the core oriented horizontally. Positioning errors are not detectable with this system.

Aluminum pressure taps were welded to the surface of the core holder. Each tap was machined to accept a Nupro 60 micron sintered filter (Swagelok, element # SS-4F-K4-60) and thereby sand migration through the tap was avoided. Pressure response was measured by a single Paroscientific pressure transducer (model 43K-101) connected to a Whitey 7-way valve (Swagelok, element # SS-43Z6). Measurement of six independent pressures is possible. The valve was switched manually and a PC was used to collect absolute pressure data from the transducer. The total acquisition time for a set of pressure data is roughly 30 to 40 s.

Nitrogen and surfactant solution are co-injected at constant rates using a Matheson 0-10 SCCM (standard cubic centimeters per minute) mass flow meter (model 8240) and an ISCO (model 500D) syringe pump, respectively. Experiments are conducted at backpressures of roughly 690 kPa (100 psi) using a Grove Mitey-Mite dome loaded backpressure regulator (Model S-91LW).

A fourth generation (1200 fixed detectors) Picker 1200 SX X-ray computed tomography (CT) scanner is used to measure porosity and the time evolution of the in-situ water saturation. Voxel dimension (analogous to pixel size in a two-dimensional image) is 0.25 mm by 0.25 mm by 5 mm. Scans were made on 13 cylindrical volume sections perpendicular to the central axis of the core. Scan locations were not evenly spaced so that scanning through pressure ports was avoided. The acquisition time of one image is 7 s and the processing time is about 40 s. The total time of measurement is short enough to capture accurately the position of the front.

Raw CT number data are converted to porosity and saturation distribution information by subtracting the CT numbers associated with given voxels. The porosity is obtained as

$$\phi = \frac{CT_{wet} - CT_{dry}}{CT_{aq} - CT_{N_2}} \quad (6)$$

where CT denotes the CT number in Hounsfields (H). The subscript *wet* corresponds to a fully aqueous-phase saturated core, *dry* a core filled with N<sub>2</sub>, *aq* denotes the CT number for the aqueous phase, and N<sub>2</sub> the CT number for the gas phase. The porosity that is determined for each voxel may be displayed as an image, averaged over the cross section, or averaged over the entire core.

To construct saturation profiles we use

$$S_w = \frac{CT_{wet} - CT_{obj}}{\phi(CT_{aq} - CT_{N_2})} \quad (7)$$

where the subscript *obj* indicates the CT value of the object being imaged and  $\phi$  is the independently measured porosity of each voxel. The measurement accuracy depends on the different parameters chosen for the X-ray emitter such as voltage, intensity, and filters. A theoretical error analysis of water saturation measurements reports that they might vary by slightly less than 6% (Akin *et al.* 1996). In practice, repeated measurement of porosity and static water saturation on this particular CT scanner, including the positioning system, displays errors of 1 to 2%.

The surfactant used to make the foamer solution is an  $\alpha$ -alpha olefin sulfonate (AOS 1416) supplied by Shell Chemical Co. Sodium chloride (NaCl) at a concentration of 0.5 wt% in distilled water was the brine. Surfactant solution concentrations employed in the experiments were 0.005, 0.01, 0.02, 0.1, and 1.0 wt% active surfactant. The less concentrated solutions were prepared by diluting the 1 wt% foamer solution with a 0.5

wt% brine. The critical micelle concentration (CMC) of the solution is roughly 0.005 wt% (Bertin *et al.* 1999) and the nominal solution viscosity is 1 mPa s.

The experimental procedure is relatively simple. The pack was prepared and mounted on the positioning system and then N<sub>2</sub> was injected to assure a dry pack. The system back pressure was increased to 690 kPa (100 psi) and dry CT scans were made at the prescribed positions. Carbon dioxide (CO<sub>2</sub>) was injected to displace the N<sub>2</sub>. At least 10 pore volumes of 0.005 wt% foamer solution were injected to saturate the pore space with liquid and satisfy adsorption of surfactant to the sand. The advantage of CO<sub>2</sub> is that it dissolves readily in water ensuring that all gas is removed. Periodically, the pressure lines were opened to purge any gas that had accumulated. Then wet CT images were collected.

The gas-liquid mixture was not foamed before injection and the injection rates are constant throughout the experiments. The foamer solution injection rate was fixed at 0.07 mL/min and the gas flow was set to 3.8 SCCM (standard cubic centimeters per minute). This translates to a superficial gas velocity of about 0.39 m/d and a gas fractional flow of 88% at the nominal system back pressure of 690 kPa. The total superficial velocity, including liquid injection, is 0.44 m/day.

Following the completion of an experiment, the core was flushed with CO<sub>2</sub> and then copious (10-20 PV) amounts of foamer solution of the next larger concentration were injected to resaturate the sandpack. The CT scanner was used to monitor the progress of resaturation thereby verifying that all gas had been ejected from the core. The experiments were performed in order of increasing surfactant concentration to assure that surfactant desorption from solid did not affect results. The first pack (6.7 μm<sup>2</sup>) was used for solutions of 0.005, 0.01, 0.02, and 1 wt% surfactant, and the second pack (7 μm<sup>2</sup>) was employed for the 0.1 wt % solution.

### 3. Experimental Summary

An overview is given of the experimental results regarding surfactant concentration and foam displacement. The experiments demonstrate that the efficiency of displacement increases with increasing surfactant solution concentration, as expected. An end effect was witnessed after gas breakthrough and is also discussed. This summary motivates an in-depth evaluation and modeling study of the experiments.

Figure 1 summarizes the cumulative water recovery for each solution concentration as measured by collecting effluent from the downstream side of the back pressure regulator. Elapsed time is given nondimensionally as pore volumes injected (PVI) which is the ratio of the total volumetric flow rate (at exit pressure) multiplied by the elapsed time and divided by the void volume of the pack. In the case of the 0.1 wt% experiment, the recovery curve was calculated by integrating the area under the water saturation profile determined by the use of CT as a function of time and adding the cumulative water injection. These saturation profiles will be described shortly. The recovery curves show an increase in the overall recovery and an increase in the time to gas breakthrough as the surfactant concentration increases. For instance, breakthrough of foam in the 0.01 wt % case occurs at about 0.60 PVI and the recovery at breakthrough is about 0.58 PV. In the case of the 1 wt% solution, the breakthrough time and the recovery at breakthrough are roughly 1.2 PVI and 1.05 PV, respectively. In Fig. 1, the cumulative injected liquid is not subtracted from the cumulative production. Also, at high surfactant concentration the pressure drops generated are large indicating gas compression. Thus, the cumulative liquid production and the breakthrough time both exceed 1 for the experiments with larger surfactant concentration.

The saturation fields across cross sections of the sandpack were computed using Eq. (7) at each scan location. Figure 2a to 2d displays typical aqueous phase saturation distributions at each of the scan locations for 1, 0.1, 0.01, and 0.005 wt% experiments, respectively. Each set of cross-sectional images was collected at about 0.5 PVI of total injection. The cross section in the upper left of each set of images is nearest the inlet. Note the shaded bars indicating the value of the aqueous-phase saturation. White indicates  $S_w$  equal to 0% whereas black indicates  $S_w$  equal to 1.

The very light gray and nearly uniform shading of Fig. 2a indicates that the foam displacement is efficient at 1 wt%. Upstream of the displacement front, the aqueous-phase saturation averages about 0.1. Also, where gas is present, it fills the entire cross section and there is no selective channeling. The images for  $x/L$  equal to 0.40 and 0.50 in Fig. 2a suggest that the saturation front is steep and sharp. The subsequent images for decreasing concentration, Figs. 2b through 2d, display similar features. However, aqueous phase saturation upstream of the front increases as the concentration decreases indicating less efficient displacement. Hence, these images corroborate the production information in Fig. 1.

The saturation change across the front becomes less sharp as the concentration decreases. For example, compare cross sections at  $x/L$  equal to 0.35 and 0.40 in Fig. 2a, 1 wt%, with the cross sections at  $x/L$  equal to 0.55 and 0.65 in Fig. 2c, 0.01 wt%. At the lower concentration, the front is more dispersed. Note that the image at  $x/L$  equal to 0.65 in Fig. 2c displays two distinct regions in the lower half of the cross section where gas has just invaded the pore space. The remaining area of the cross section is filled with aqueous solution. Figure 2d, for the 0.005 wt% concentration, displays the least uniform sweep pattern. In the fifth and sixth images ( $x/L = 0.35$  and  $0.40$ ) of Fig. 2d, it is apparent that a portion of the aqueous phase solution is not displaced from the top of the sandpack.

All of the experiments proceeded as expected prior to breakthrough. After breakthrough, evidence of end effects was witnessed in both the saturation distributions and in pressure profiles. Figure 3 presents the steady-state, one-dimensional, aqueous-phase saturation profiles as a function of distance along the pack. The saturation values were obtained by determining the water saturation in each voxel of a cross section and then averaging. Different symbols indicate experiments at different surfactant concentration and the dashed lines merely connect the individual points. For the 1 and 0.1 wt% experiments, the steady aqueous phase saturation is below 0.15 and relatively uniform throughout the sand pack. At the lower concentrations (0.02, 0.01, and 0.005 wt%), the aqueous phase saturation is clearly larger near the outlet than it is in the center of the column. The effect becomes more pronounced as surfactant solution concentration decreases. This signifies a classic capillary end effect where the porous medium retains water in an attempt to maintain equilibrium across the outlet where the capillary pressure is zero or near zero (Perkins 1957; Douglas and Wagner 1958; Kyte and Rapoport 1958).

A second type of end effect, or a different manifestation of a capillary end effect, was witnessed in the high surfactant concentration experiments, as illustrated in Fig. 4 for 1 wt% solution. Here the pressure-drop profile along the length of the core is plotted as a function of time. Different symbols are associated with different times and dashed lines connect pressure data points to guide the eyes. As indicated by the figure, the gas breakthrough time is between 1.2 and 1.4 PVI. Pressure gradients prior to breakthrough are always steepest in the foam-filled region and shallowest in the aqueous-phase filled region. After breakthrough, the steepest pressure gradients are found near the outlet. Comparing profiles at times of 1.4, 2.9, and 6.5 PVI, it is found that region of the pack where the pressure gradient is steepest expands from the outlet toward the inlet. At 1.4 PVI, the pressure gradient is steepest between  $x/L$  equal to 0.7 and 1, whereas at 1.9 PVI, the steep gradient extends from  $x/L$  equal to 0.45 to 1. At 6.5 PVI, the pressure drop over

the pack is about 580 kPa (84 psi). The experiments at 0.1 wt% concentration display a similar behavior post breakthrough although not shown here.

An additional feature is the length of time to achieve a steady-state pressure profile. Previous experiments in sandstone with AOS at about 1 wt% concentration employing similar injection rates reached steady state in about 2 PVI (Kovscek *et al.* 1995). The long time to reach steady state in the current experiments results because the pressure drop across the core builds from the outlet toward the inlet. Since this occurs against the direction of flow, it is a slow process.

#### **4. Transient Displacements**

To model the transient foam displacements, Eqs. (1) through (5) are solved with a standard fully-implicit, simultaneous-solution finite difference method with upstream weighting of the phase mobilities (Aziz and Settari 1979). Additionally, water and nitrogen mass balances are computed. Since the sand packs are presaturated with surfactant solution, there is no need to compute a surfactant mass balance. The primary variables are water-phase pressure, gas-phase saturation, and bubble density. Boundary and initial conditions mirror the experiments: gas and liquid are injected at constant mass rates and the outlet pressure is fixed at 690 kPa (100 psi). The surfactant and gas are not foamed before injection. Therefore, no bubbles are injected and  $Q_b$  is set to zero. The initial conditions include  $S_w$  equal to 1,  $n_f$  equal to 0, and the appropriate uniform surfactant concentration depending upon the experiment under consideration.

Tables 1 and 2 list the model parameters including standard multiphase flow information as well as population balance parameters. Also given in Table 1 is the capillary pressure versus water saturation function (Pruess 1987). The parameter  $\alpha$  in the expression for effective foam viscosity varies with surface tension (Hirasaki and Lawson 1985). As Table 2 shows, the surface tension changes by only 2.9 mN/m over the entire range of concentrations employed. Accordingly,  $\alpha$  is held fixed in the simulations to follow. The ratio of foam generation to coalescence rate constants,  $k_1/k_{-1}^*$ , was chosen to yield bubbles with undistorted spherical radii of about 0.4 mm for the 1 wt% case. Further information on parameter estimation for population balance models is discussed in some detail elsewhere (Kovscek and Radke 1994; Kovscek *et al.* 1995).

The critical capillary pressure,  $P_c^*$ , as a function of surfactant concentration is required to simulate the experiments. Because the surfactant concentration in each experiment is constant, we set  $P_c^*$  at each concentration rather than assuming a functional form for  $P_c^*$  versus surfactant concentration. Table 2 lists the value of  $P_c^*$  found for each concentration and the experimentally determined surface tension as a function of concentration for this particular surfactant at a brine concentration of 0.5 wt%. As expected,  $P_c^*$  is large when the surfactant concentration is large and decreases as the concentration approaches the CMC (Aronson *et al.* 1994).

The modeling results for foam texture evolution at each surfactant concentration are presented first. Unfortunately, no experimental method exists to measure directly foam texture in situ. High surfactant concentration results are shown first and then subsequent simulations at lower concentration follow. Next, the effect of foam texture on gas mobility is judged from measured and computed aqueous-phase saturation profiles as a function of time. Pressure drop profiles and the match between experiment and model complete this section.

## 4.1 Foam Texture

The predicted bubble concentration along the length of the core as a function of time is given for each of the different surfactant concentrations in Fig. 5. Figure 5a represents the largest concentration while Fig. 5e shows the lowest. Time is given nondimensionally in pore volumes of total injection with the exit pressure used to calculate the volumetric gas rate. In Fig 5a, representing the 1 wt% concentration experiment, a region of net generation is found near the inlet. Bubble concentration is nearly constant at all time levels beyond roughly the first quarter of the sand pack until the concentration peaks immediately upstream of the front. Physically, the net rate of foam generation is large at the front. Thus, the bubble concentration goes through a maximum before decreasing to zero downstream of the front where there is no gas, and hence, no bubbles (Kovscek *et al.* 1997). The relatively constant foam concentration between the inlet region and the foam front is about 22 bubbles/ mm<sup>3</sup>. A foam bubble of this size has a diameter of roughly 0.44 mm when taken out of the porous medium and allowed to assume a spherical shape. For the simulation of the 1 wt% concentration, the breakthrough time of bubbles is about 1.2 PVI. This agrees well with the cumulative liquid production information in Fig. 1.

The bubble concentration profiles shown in Fig. 5b for the 0.1 wt% concentration are lower than the values for the 1 wt% case. The lower surfactant concentration results in a lesser critical capillary pressure for foam coalescence, as given in Table 2. As a result, the foam coalescence rate increases and the average bubble concentration decreases. Disregarding the inlet region and the elevation of bubble concentration at the front, the flowing bubble concentration in this case is about 3.5 bubbles/ mm<sup>3</sup> corresponding to an undistorted spherical bubble diameter of 0.82 mm.

For the lowest concentrations in Figs. 5c through 5e, the bubble concentration gradually approaches zero with declining surfactant concentration. In Fig. 5c for the 0.02

wt% case, the texture upstream of the spike in bubble concentration at the front is only 0.4 bubbles/ mm<sup>3</sup> while in Figs. 5d and 5e for the 0.01 and 0.005 wt% solutions, the bubble concentration in this region is essentially zero ( $20 \times 10^{-8}$  mm<sup>-3</sup>). The spherical bubble diameters corresponding to these textures are 1.7 mm for the 0.02 wt% case and essentially infinite for the smallest concentrations. In the limit of no foam, continuous gas results and infinitely large bubbles emerge.

An elevation in foam texture in the region of the front is also found in the lower surfactant concentration cases. The process of snap-off of gas bubbles is purely a mechanical process and continues regardless of the concentration of surfactant. This is reflected in the net foam generation rate of Eq. (1). As a consequence, bubbles are always generated when the water saturation is high and the capillary pressure is less than critical such as when gas first enters a water saturated region of the porous medium. Foam coalescence forces quickly destroy most of this initial foam because the surfactant concentration is low and thus the limiting capillary pressure for foam coalescence is reached quickly. Correspondingly, the magnitude of the elevation in foam texture at the front also decreases with decreasing surfactant concentration. In Fig. 5c the maximum texture is 8 bubbles/ mm<sup>3</sup> while in Fig. 5d it is 4 bubbles/ mm<sup>3</sup>. There is little difference in the bubble texture profiles of Figs. 5d and 5e because the limiting capillary pressure, as given in Table 2, has changed little between these two cases.

## **4.2 Aqueous Phase Saturation**

The one-dimensional aqueous-phase saturation profiles as a function of time for each case are presented in Fig. 6. Time is again given nondimensionally in pore volumes. One dimensional saturation data is obtained by averaging the voxel by voxel CT-measured saturations for each cross section. In Fig. 6, symbols give the experimentally

measured points and they are connected by dashed lines to guide the eye. The solid lines represent model predictions based upon the foam textures in Fig. 5 and Eqs. (3) to (5) for gas mobility. In general, transient displacement is efficient where bubble concentrations are large such as in the 1 wt% surfactant concentration case in Fig. 6a, and displacement efficiency decreases as surfactant concentration and bubble texture decrease. Also note that the saturation change across the front is steep and sharp when the foam is strong as shown in Figs 6a and 6b.

The match between experiment and model is quite good in all cases prior to breakthrough and the onset of end effects, except perhaps the 0.005 wt% case. Displacement efficiency declines with decreasing surfactant solution concentration in both the simulations and experiments. Also, notice that the predicted saturation profiles across the displacement front in Figs. 6c through 6e become more diffuse as the surfactant concentration decreases. Predictions echo experiments in this regard. It is important to recall that these results are not achieved by history matching each experiment. The only parameter that changes in each simulation is the value of  $P_c^*$ . This parameter is physical and directly related to surfactant concentration (Aronson *et al.* 1994).

The experimental displacement results summarized in Fig. 6e show a region at  $x/L$  roughly equal to 0.35 where desaturation of the aqueous phase is inefficient. The aqueous phase saturation distribution at this cross section of the sandpack is illustrated in the image at  $x/L$  equal to 0.35 in Fig. 2d. Displacement is not uniform across the cross section, and a region of 100 % aqueous phase saturation remains in the upper portion of the cross section. The simulations are one dimensional and cannot account for such selective displacement at low surfactant concentration. Nevertheless, the simulations reproduce, qualitatively, the low displacement efficiency at this surfactant concentration.

Capillary end effects are evident in the evolution of the experimental water saturation profile in Figs. 6d and 6e. In Fig. 6d, breakthrough of gas at the outlet occurs between 0.4 and 0.6 PVI. Following breakthrough there is little desaturation of the final third of the core; the saturation data at 0.6 and 1 PVI in this region nearly overlay each other. Similar behavior is found for the 0.005 wt% experiment. The foam simulations do not incorporate end effects and so cannot match the post breakthrough saturation distributions.

### **4.3 Pressure Drop**

The second type of in-situ data collected was pressure drop. The lower limit of accuracy for the pressure measurement system used is about 0.14 to 0.34 kPa (0.02 to 0.05 psi). Experimental and simulated pressure drop profiles as a function of time are presented in Fig. 7 for each of the surfactant concentrations. The match between model and experiment is acceptable. Large bubble concentrations lead to significant gas-phase flow resistance and low aqueous-phase saturation. Therefore, the 1 wt% case with the finest bubble texture, as shown in Fig. 5a, demonstrates the largest overall pressure drop. As the bubble textures decline with surfactant concentration, the predicted pressure drops decline also.

For the 1 wt% and 0.1 wt% cases in Figs. 7a and 7b where significant foam and pressure drops are generated, it is easy to distinguish the foam-filled region of the sand pack in the pressure drop profiles. For example in Fig. 7b at 0.41 PVI, a relatively steep pressure gradient due to the presence of foam extends from the inlet to  $x/L$  equal to 0.43. The pressure drop in the remainder of the sand pack is small corresponding to the single-phase flow of water.

To improve the clarity of Figs. 7c to 7e, a legend displays the symbol and time corresponding to each experimental data point. Difficulties were encountered in

measuring the small pressure drops characteristic of the lower surfactant concentrations, especially at the inlet of the sandpack. Gas migrated into some of the pressure lines during the experiment. In these instances, large, aphysical, positive pressure gradients were measured. These erroneous pressure data likely originated from gas entering the sintered filters inside the pressure taps. Accordingly, erroneous pressure information has been deleted from Figs. 7d and 7e. The portion of the data presented in Fig. 7c that is in error is not clear, so all information is retained. Despite these problems, experiment and simulation agree on the general magnitude of pressure drop.

A feature of the model that bears further discussion is the predicted pressure drop profiles for the low surfactant concentration cases in the region immediately upstream of the foam front. Examine the pressure profile at 0.44 PVI in Fig. 7c and the corresponding bubble concentration profile in Fig. 5c. The pressure gradient is relatively shallow in the foam-filled region except immediately before the front. Here, the gradient is much steeper than in the front region because bubble concentration is elevated at the front. This elevation in texture reduces gas mobility causing the pressure gradient to steepen.

## **5. End Effect**

The end effect evident in the saturation profiles of Fig. 3 for low surfactant concentrations (0.005, 0.01, and 0.02 wt%) is similar in origin to the capillary end effects described elsewhere for regular two-phase flow (Perkins 1957; Douglas and Wagner 1958; Kyte and Rapoport 1958). Hence, we do not attempt to analyze this effect here. It is far less clear why the pressure gradient steepens from the outlet against the direction of flow toward the inlet, as illustrated in Fig. 4 for the 1 wt% concentration case. The

steady aqueous-phase saturation profiles given in Fig. 3 for the 0.1 and 1 wt% cases demonstrate very low  $S_w$  near the sand pack outlet and so do not appear to be classic capillary end effects. Of course, there are no measurements at  $x/L$  equal to 1 and  $S_w$  might increase immediately before the outlet.

We will use the population balance approach and some simplifying assumptions drawn from the experimental results to probe the origin of the end effect witnessed at 0.1 and 1 wt% surfactant concentrations. First, the Darcy velocity of the compressible

foamed gas phase is written as

$$u_f = \frac{p_{sc} u_{f,sc}}{p_g} = \frac{-kk_{rf}}{\mu_f} \frac{dp_g}{dx} \quad (8)$$

where the subscript  $sc$  indicates standard conditions. For large foam bubble concentration, such as the 1 and 0.1 wt% concentration experiments, the gas viscosity contribution in Eq. (3) for effective foam viscosity is negligible and

$$\mu_f = \frac{\alpha n_f}{u_f^{1/3}} (\phi X_f S_g)^{1/3} \quad (9)$$

In Eq. (9), the interstitial velocity has been replaced by  $u_f/\phi X_f S_g$ . Some knowledge of the foam texture is necessary to employ Eq. (9) in Eq. (8). Recall, that roughly 6 PVI are required for the pressure to reach a steady state. Thus, the conditions within the core evolve quite slowly after gas breakthrough and local equilibrium can be assumed to hold. Setting the expression for the net generation of foam in Eq. (1) to zero, replacing interstitial velocity with Darcy velocity and the appropriate phase saturations, and solving for foam texture, one obtains

$$n_f = \left( \frac{k_1}{k_{-1}} \right) \left( \frac{u_w}{\phi S_w} \right) \left( \frac{\phi X_f S_g}{u_f} \right)^{2/3} \quad (10)$$

Substituting Eqs. (9) and (10) into Eq. (8), recognizing that  $p_{sc}u_{f,sc}$  equals  $p_g u_f$ , and integrating with respect to pressure yields

$$\frac{k_{rf}}{X_f S_g} = \Delta x \left( \frac{\alpha k_1}{k k_{-1}} \right) \left( \frac{u_w}{S_w} \right) \frac{1}{\Delta p_g} \quad (11)$$

where  $\Delta p_g$  is the pressure drop and  $\Delta x$  the distance between measurement points. Of the quantities in Eq. (11),  $\Delta p_g$ ,  $S_g$ ,  $S_w$ ,  $u_w$ ,  $k$ , and  $\Delta x$  are directly measurable;  $\alpha$  and  $k_1$  are assumed to be equal to their values in Table 1; and  $k_{rf}$  and  $k_{-1}$  are functions of the unknown  $X_f$  and measured  $S_g$ . Thus, the only unknown quantity in Eq. (11) is the flowing foam fraction,  $X_f$ .

Figure 8 displays the result of applying Eq. (11) to the pressure information in Fig. 4 and the CT-scan determined phase saturations. The step changes in  $X_f$  evident in the profiles of Fig. 8 are a result of the pressure drop measurements over discrete regions of the sandpack. On average, the flowing fraction is about 0.04 at steady state, 5.2 PVI. Near the outlet the flowing foam fraction is low at all times. Progressively, the flowing foam fraction decreases between 1.3 and 5.2 PVI. As indicated by Eqs. (4b) and (5), foam relative permeability decreases as  $X_f$  decreases and the pressure drop correspondingly increases. Reductions in  $X_f$  occur first near the outlet and at later times near the inlet. Thus, pressure gradients increase first in the vicinity of the outlet.

Near the inlet, net foam generation occurs, as shown in Figs. 5(a) and 5(b). The application of local equilibrium to this region is not appropriate. Accordingly, flowing foam fraction between the first two pressure taps was not computed.

Figure 9 displays the results of applying this analysis to the results of the 0.1 wt% concentration experiment. Again,  $X_f$  decreases slowly over time and reductions occur first at the outlet and progress toward the inlet.

## 6. Conclusion

An experimental study of foam generation and propagation as a function of aqueous surfactant concentration was conducted in  $7 \mu\text{m}^2$ , homogeneous sand packs. The in-situ phase saturation and pressure distribution were measured during the experiments. As expected, it is found that displacement efficiency decreases and gas mobility increases with decreasing surfactant concentration. This experimental trend indicates that foam weakens as the surfactant concentration decreases. However, even weak foam improves displacement somewhat.

Such results are best understood considering the role of foam bubble size, or synonymously foam texture, in setting the mobility of foamed gas in porous media. Many small bubbles result in a low mobility foam and few large bubbles result in a high mobility foam. Foam bubbles, at fixed injection rates of liquid and gas, grow in volume as surfactant concentration decreases because foam coalescence forces are inversely proportional to surfactant concentration.

These ideas are expressed quantitatively by the incorporation of the role of foam texture on displacement in porous media using a mechanistic, mean, bubble-size conservation equation. In essence, foam is treated as a nonchemical, reactive, component of the gas phase and the evolution of foam texture is modeled explicitly using rate equations for foam generation and coalescence. Coalescence as a function of surfactant concentration is modeled employing the notion of limiting capillary pressure for foam stability. That is, the maximum suction capillary pressure that foam films can withstand decreases with surfactant concentration. The foam bubble population balance model predicts accurately the location of saturation and pressure fronts across the range of concentrations studied. This is achieved by properly accounting for limiting capillary

pressure as a function of aqueous surfactant concentration and without parameter adjustment.

The post breakthrough behavior exhibited in the experiments indicates the presence of an end effect. The end effect is similar to a classic capillary end effect for low surfactant concentration. At larger concentrations, the end effect results in the pressure gradient building from the outlet, against the direction of flow, toward the inlet. Many pore volumes of fluid injection are necessary to achieve steady state even at moderate to high surfactant concentrations and these long times are attributed to such end effects.

## Nomenclature

$CT$	CT number (Hounsfields)
$k$	permeability ( $m^2$ )
$k$	rate constant (units vary, see subscripts)
$k_r$	relative permeability (dimensionless)
$n$	number density of foam ( $m^{-3}$ )
$p$	pressure (Pa)
$P_c$	capillary pressure (Pa)
PV	dimensionless volume
PVI	dimensionless time
$Q_b$	source/sink term for bubbles ( $m^{-3}s^{-1}$ )
$S$	phase saturation (dimensionless)
$t$	time (s)
$u$	Darcy phase velocity (m/s)
$v$	interstitial phase velocity (m/s)
$x$	distance (m)
$X$	foam fraction (dimensionless)

### *subscripts*

$l, -l$	generation, coalescence rate constant ( $s^{1/2}m^{-13/3}, m^{-1}$ )
$a,b$	exponents for phase relative permeability
$aq$	CT number for the aqueous phase
$d$	normalized phase saturation
$dry$	CT number for dry porous medium
$f$	flowing foam
$g$	gaseous phase
$N_2$	CT number for nitrogen
$obj$	CT number, general
$ir$	irreducible phase saturation
$t$	trapped or immobile foam
$w$	aqueous phase
$wet$	CT number for wet porous medium

### *superscripts*

$o$	reference value
*	limiting capillary pressure

*Greek*

$\alpha$	proportionality constant ( $\text{Pa}\cdot\text{s}^{2/3}\cdot\text{m}^{10/3}$ )
$\phi$	porosity (dimensionless)
$\sigma$	surface tension (N/m)
$\mu$	viscosity (Pa-s)

## References

1. Aarra, M. G., Skauge, A., Sognesand, S. and Stenhaug, M. (1996). "A Foam Pilot Test Aimed at Reducing Gas Inflow in a Production Well at the Oseberg Field." Petroleum Geoscience **2**: 125-132.
2. Akin, S., Demiral, M. R. B. and Okandan, E. (1996). "A Novel Method of Porosity Measurement Utilizing Computerized Tomography." In Situ **20**(4): 347-365.
3. Aronson, A. S., Bergeron, V., Fagan, M. E. and Radke, C. J. (1994). "The Influence of Disjoining Pressure on Foam Stability and Flow in Porous Media." Colloids and Surfaces A: Physicochemical Eng. Aspects **83**: 109-120.
4. Aziz, K. and Settari, A. (1979). Petroleum Reservoir Simulation. London, Applied Science Publishers LTD.
5. Bergeron, V. and Radke, C. J. (1992). "Equilibrium Measurements of Oscillatory Disjoining Pressures in Aqueous Foam Films." Langmuir **8**(12): 3020-3026.
6. Bergeron, V., Fagan, M. E. and Radke, C. J. (1993). "Generalized Entering Coefficients - A Criterion for Foam Stability Against Oil in Porous Media." Langmuir **9**(7): 1704-1713.
7. Bernard, G. G., Holm, L. W. and Jacobs, L. W. (1965). "Effect of Foam on Trapped Gas Saturation and on Permeability of Porous Media to Gas." Soc. Pet. Eng. J. **5**(4): 295-300.
8. Bertin, H. J., Apaydin, O. G., Castanier, L. M. and Kovscek, A. R. (1999). "Foam Flow in Heterogeneous Porous Media: Effect of Crossflow." Soc. Pet. Eng. J. **4**(2): to appear.
9. Bretherton, F. P. (1961). "The Motion of Long Bubbles in Tubes." J. Fluid Mech. **10**: 166-188.
10. Chambers, K. T. and Radke, C. J. (1991). Capillary Phenomena in Foam Flow Through Porous Media. Interfacial Phenomena in Petroleum Recovery. N. R. Morrow. New York, Marcel Dekker Inc. **Ch. 6**: 191-255.

11. Cohen, D., Patzek, T. W. and Radke, C. J. (1997). "Onset Of Mobilization and The Fraction OF Trapped Foam In Porous Media." Transport in Porous Media **28**(3): 253-284.
12. De Vries, A. S. and Wit, K. (1990). "Rheology of Gas/Water Foam in the Quality Range Relevant to Steam Foam." Soc. Pet. Eng. Res. Eng. **5**(2): 185-192.
13. Douglas, J. J. and Wagner, R. J. (1958). "Calculation of Linear Waterflood Behavior Including the Effects of Capillary Pressure." Petroleum Transactions, AIME **213**: 96-102.
14. Ettinger, R. A. and Radke, C. J. (1992). "Influence of Foam Texture on Steady Foam Flow in Berea Sandstone." Soc. Pet. Eng. Res. Eng. **7**(1): 83-90.
15. Friedmann, F., Chen, W. H. and Gauglitz, P. A. (1991). "Experimental and Simulation Study of High-Temperature Foam Displacement in Porous Media." Soc. Pet. Eng. Res. Eng. **6**(1): 37-45.
16. Gillis, J. V. and Radke, C. J. (1990). "A Dual-Gas Tracer Technique for Determining Trapped Gas Saturation During Steady Foam Flow in Porous Media". SPE 20519, at 65th SPE Annual Technical Conference, New Orleans, LA, (September 23-26).
17. Hanssen, J. E. (1993a). "Foam as a Gas-Blocking Agent in Petroleum Reservoirs. I: Empirical Observations and Parametric Study." Journal of Petroleum Science & Engineering **10**(2): 135-156.
18. Hanssen, J. E. (1993b). "Foam as a Gas-Blocking Agent in Petroleum Reservoirs. II: Mechanisms of Gas Blockage." Journal of Petroleum Science & Engineering **10**(2): 135-156.
19. Hirasaki, G. J. (1991). Thermodynamics of Thin Films and The Three-Phase Contact Regions. in Interfacial Phenomena in Petroleum Recovery. N. R. Morrow, ed., New York, Marcel Dekker Inc. **36**: 23-76.
20. Hirasaki, G. J. and Lawson, J. B. (1985). "Mechanisms of Foam Flow in Porous Media: Apparent Viscosity in Smooth Capillaries." Soc Pet. Eng. J. **25**(2): 176-190.

21. Hirasaki, G. J., Miller, C. A., Szafranski, R., Lawson, J. B. and Akiya, N. (1997). "Surfactant/Foam Process for Aquifer Remediation". SPE 37257, at SPE International Symposium on Oilfield Chemistry, Houston, TX, Feb 18-21 .
22. Hirasaki, G. J., Miller, C. A., Szafranski, R., Lawson, J. B., Tanzil, D., Jackson, R. E., Londergan, J. and Meinardus, H. (1997). "Field Demonstration of the Surfactant/Foam Process for Aquifer Remediation". SPE 39393, at SPE Ann. Tech. Conf. and Exhibition, San Antonio, TX, Oct 5-8 .
23. Hoefner, M. L., Evans, E. M., Buckles, J. J. and Jones, T. A. (1994). "CO<sub>2</sub> Foam: Results from Four Developmental Field Trials". SPE/DOE 27787, at SPE/DOE Ninth Symposium on Improved Oil Recovery, Tulsa, Oklahoma, April 17-20 .
24. Holm, L. W. (1968). "The Mechanism of Gas and Liquid Flow Through Porous Media in the Presence of Foam." Soc. Pet. Eng. J. **8**(4): 359-369.
25. Huh, D. G. and Handy, L. L. (1989). "Comparison of Steady- and Unsteady-State Flow of Gas and Foaming Solution in Porous Media." Soc. Pet. Eng. Res. Eng. **4**(1): 77-84.
26. Jiménez, A. I. and Radke, C. J. (1989). Dynamic Stability of Foam Lamellae Flowing Through a Periodically Constricted Pore. in Oil-Field Chemistry: Enhanced Recovery and Production Stimulation. J. K. Borchardt and T. F. Yen, eds., Washington, D.C., American Chemical Society. **396**: 460-479.
27. Kharabaf, H. and Yortsos, Y. C. (1998). "Pore Network Model for Foam Formation and Propagation in Porous Media." Soc. Pet. Eng. J. **3**(1): 42-53.
28. Khatib, Z. I., Hirasaki, G. J. and Falls, A. H. (1988). "Effects of Capillary Pressure on Coalescence and Phase Mobilities in Foams Flowing Through Porous Media." Soc. Pet. Eng. Res. Eng. **3**(3): 919-926.
29. Kovscek, A. R., Patzek, T. W. and Radke, C. J. (1995). "A Mechanistic Population Balance Model For Transient and Steady-State Foam Flow in Boise Sandstone." Chem. Eng. Science **50**(23): 3783-3799.
30. Kovscek, A. R., Patzek, T. W. and Radke, C. J. (1997). "Mechanistic Foam Flow Simulation in Heterogeneous Multidimensional Porous Media." Soc. Pet. Eng. J. **2**(4): 511-526.

31. Kovscek, A. R. and Radke, C. J. (1994). Fundamentals of Foam Transport in Porous Media. in Foams in the Petroleum Industry. L. L. Schramm, ed., Washington, D.C., American Chemical Society. **242**: 115-163.
32. Kovscek, A. R. and Radke, C. J. (1996). "Gas Bubble Snap-Off Under Pressure-Driven Flow in Constricted Noncircular Capillaries." Colloids and Surfaces A: Physicochemical and Engineering Aspects **117**: 55-76.
33. Kyte, J. R. and Rapoport, L. A. (1958). "Linear Waterflood Behavior and End Effects in Water-Wet Porous Media." Petroleum Transactions, AIME **213**: 423-426.
34. Myers, T. J. and Radke, C. J. (1999). "Transient Foam Displacement in the Presence of Residual Oil: Experiment and Simulation Using a Population-Balance Model.". SPE 56412, at SPE Ann. Tech. Conf. and Exhibition, Houston, TX, (October 3-6) .
35. Patzek, T. W. (1996). "Field Application of Steam Foam for Mobility Improvement and Profile Control." Soc. Pet. Eng. Res. Eng. **11**(2): 79-85.
36. Perkins, F. M. J. (1957). "An Investigation of the Role of Capillary Forces in Laboratory Waterfloods." Petroleum Transactions, AIME **210**: 409-411.
37. Persoff, P., Radke, C. J., Pruess, K., Benson, S. M., and Witherspoon, P. A. (1991) "A Laboratory Investigation of Foam Flow in Porous Media at Elevated Pressures," Soc. Pet. Eng. Res. Eng. **6**(3), 365-371.
38. Pruess, K. (1987) "TOUGH User's Guide," Rep NUREG/CR-4645, Nucl. Reg. Commission, Washington D.C.
39. Rossen, W. R. (1995). Foams in Enhanced Oil Recovery. in Foams: Theory, Measurements and Applications. R. K. Prud'homme and S. Khan, eds, Surfactant Science Series, Vol 57, Marcel Dekker, Inc, New York.
40. Rossen, W. R. and Gauglitz, P. A. (1990). "Percolation Theory and Mobilization of Foams in Porous Media." Am. Inst. Chem. Eng. J. **37**(8): 1176-1188.

41. Sanchez, J. M., Schechter, R. S. and Monsalve, A. (1986). "The Effect of Trace Quantities of Surfactant on Nitrogen/Water Relative Permeabilities". SPE 15446, at 61st SPE Annual Technical Conference, New Orleans, LA, (October 5-8) .
42. Saraf, D. N. and Fatt, I. (1967). "Three-Phase Relative Permeability Measurement Using a Nuclear Magnetic Resonance Technique for Estimating Fluid Saturation." Soc. of Pet. Eng. J. **9**: 235-242.
43. Stone, H. L. (1970). "Probability Model for Estimating Three-Phase Relative Permeability." J. Pet. Tech. **22**(2): 214-218.
44. Vrij, A. (1966). "Possible Mechanism for the Spontaneous Rupture of Thin, Free Liquid Films." Disc. Faraday Soc. **42**: 22-33.
45. Wong, H., Radke, C. J. and Morris, S. (1995). "The Motion of Long Bubbles in Polygonal Capillaries: I. Thin Films." J. Fluid Mech. **292**: 71-95.
46. Wong, H., Radke, C. J. and Morris, S. (1995). "The Motion of Long Bubbles in Polygonal Capillaries: II. Drag, Fluid Pressure, and Fluid Flow." J. Fluid Mech. **292**: 95-110.
47. Wunderlich, R. W., Fountain, J. C. and Jackson, R. E. (1992). "In Situ Remediation of Aquifers Contaminated with Dense Nonaqueous Phase Liquids by Chemical Enhanced Solubilization." J. Soil Contamination **1**(4): 361-378.

Table 1. Parameter Values.

Two-phase flow parameters		Population balance parameters	
parameter	value	parameter	value
k	7 $\mu\text{m}^2$	$k_1$	$7.5 \times 10^{12} \text{ s}^{1/2} \text{ m}^{-13/3}$
$\phi$	0.35	$k_{-1}^o$	100 $\text{m}^{-1}$
a	3	$\alpha$	$2.5 \times 10^{-14} \text{ Pas}^{2/3} \text{ m}^{10/3}$
b	1.8	$X_f$	0.10
$k_{rw}^o$	0.7		
$k_{rg}^o$	1	Capillary pressure function after Pruess (1987)	
$S_{wir}$	0.06	$P_c = \sigma \sqrt{\frac{\phi}{k}} (1.417(1 - S_{wd}) - 2.120(1 - S_{wd})^2 + 1.263(1 - S_{wd})^3)$	
$\mu_w$	1.0 mPa-s		
$\mu_g$	0.018 mPa-s		

Table 2. Limiting Capillary Pressure and Surface Tension Values ( $\sigma$  from Bertin *et al.* (1999)).

Concentration (wt%)	$\sigma$ (mN/m)	$P_c^*$ (kPa)
1.0	31.1	30.4
0.10	31.9	17.6
0.020	32.8	7.19
0.010	33.1	3.67
0.005	34.0	2.34

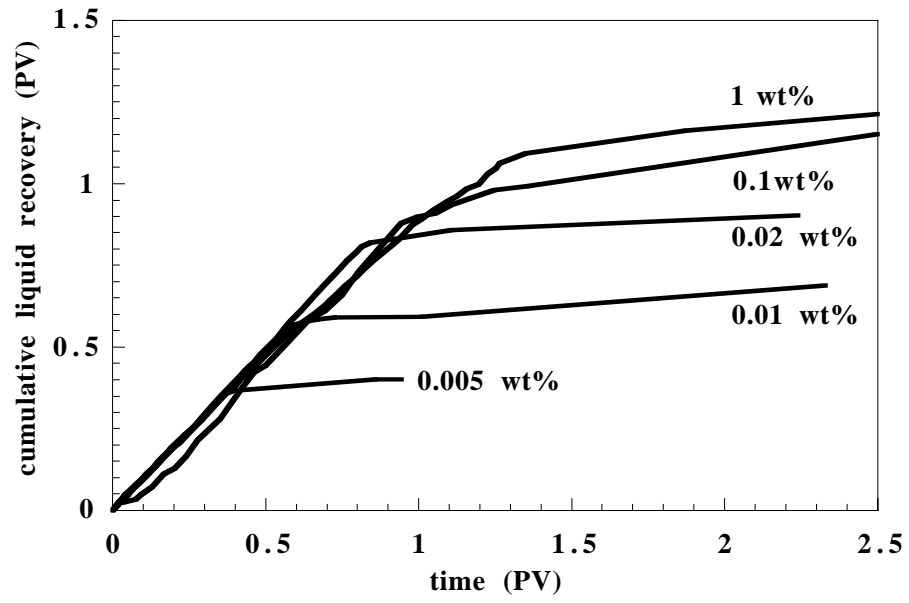
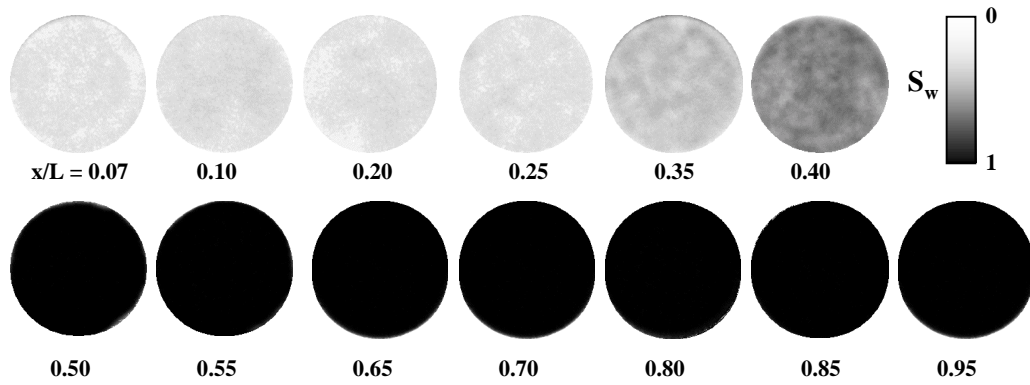
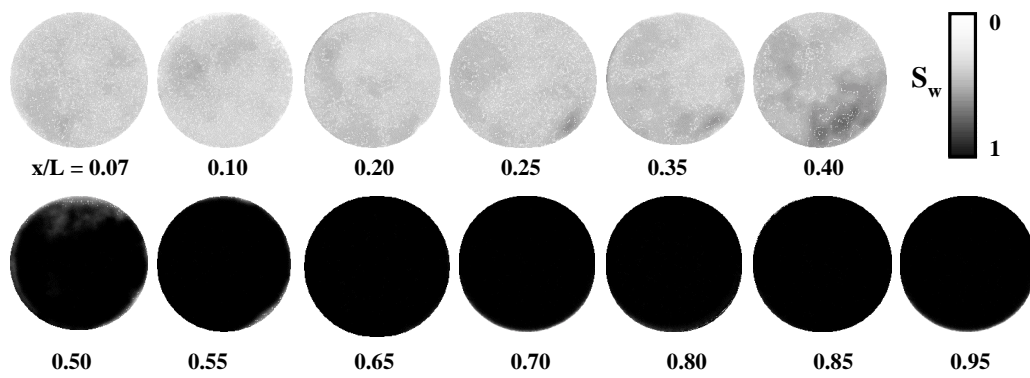


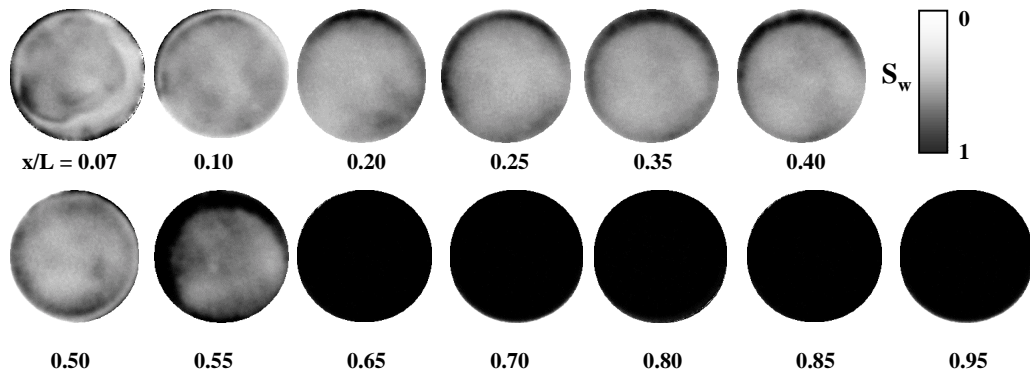
Figure 1. Cumulative water recovery.



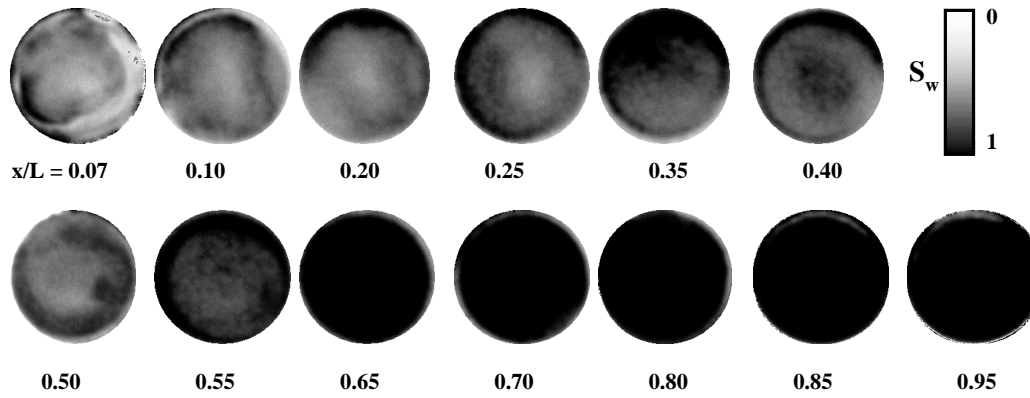
(a)



(b)



(c)



(d)

**Figure 2. Water saturation in cross sections along the length of the sandpack. Below each image the position of the cross section is given (a) 1 wt% case at 0.52 PVI; (b) 0.1 wt% case at 0.51 PVI; (c) 0.01 wt% case at 0.51 PVI; (d) 0.005 wt% case at 0.55 PVI.**

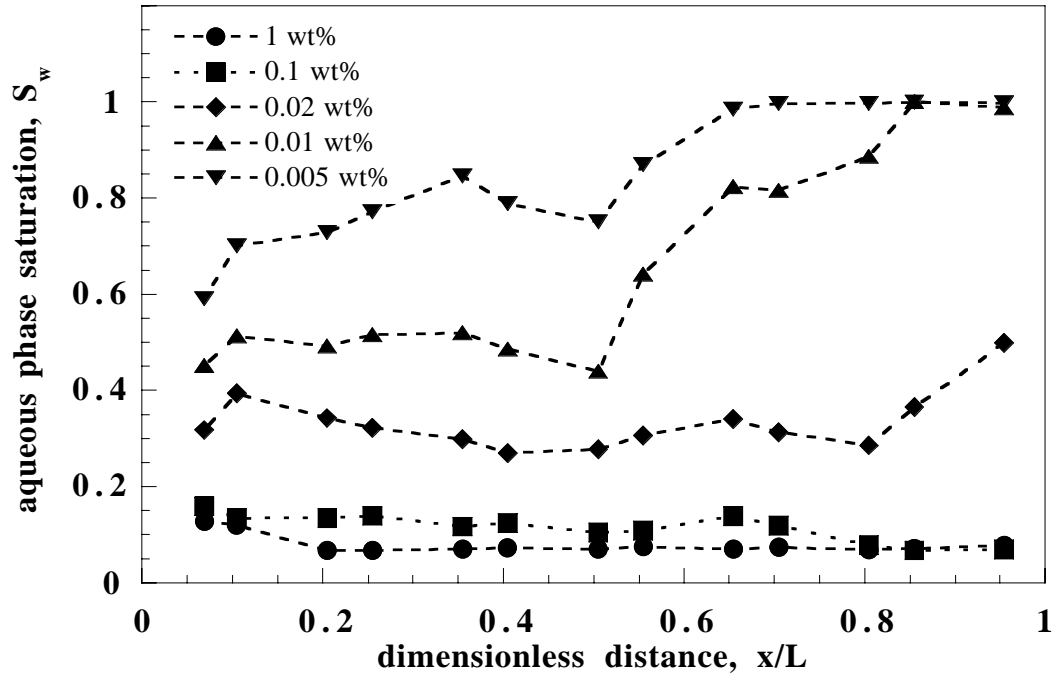


Figure 3. Steady state aqueous-phase saturation profiles.

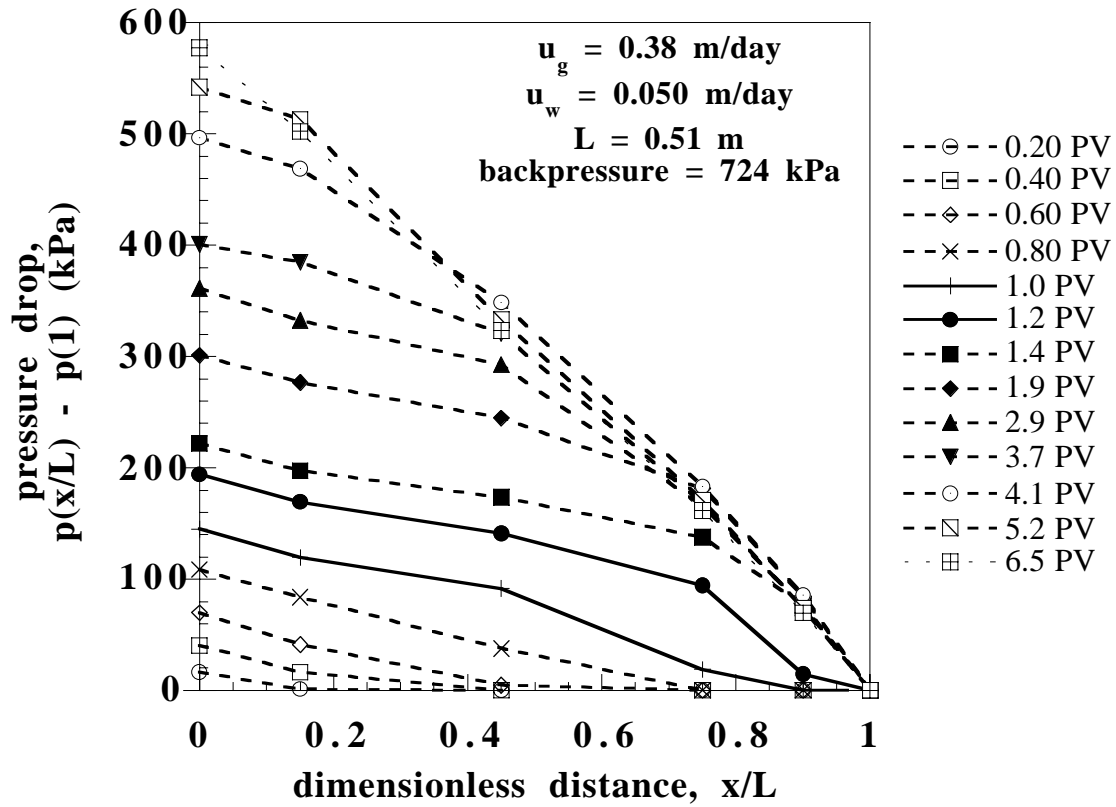


Figure 4. Experimental transient pressure profiles, 1 wt% case.

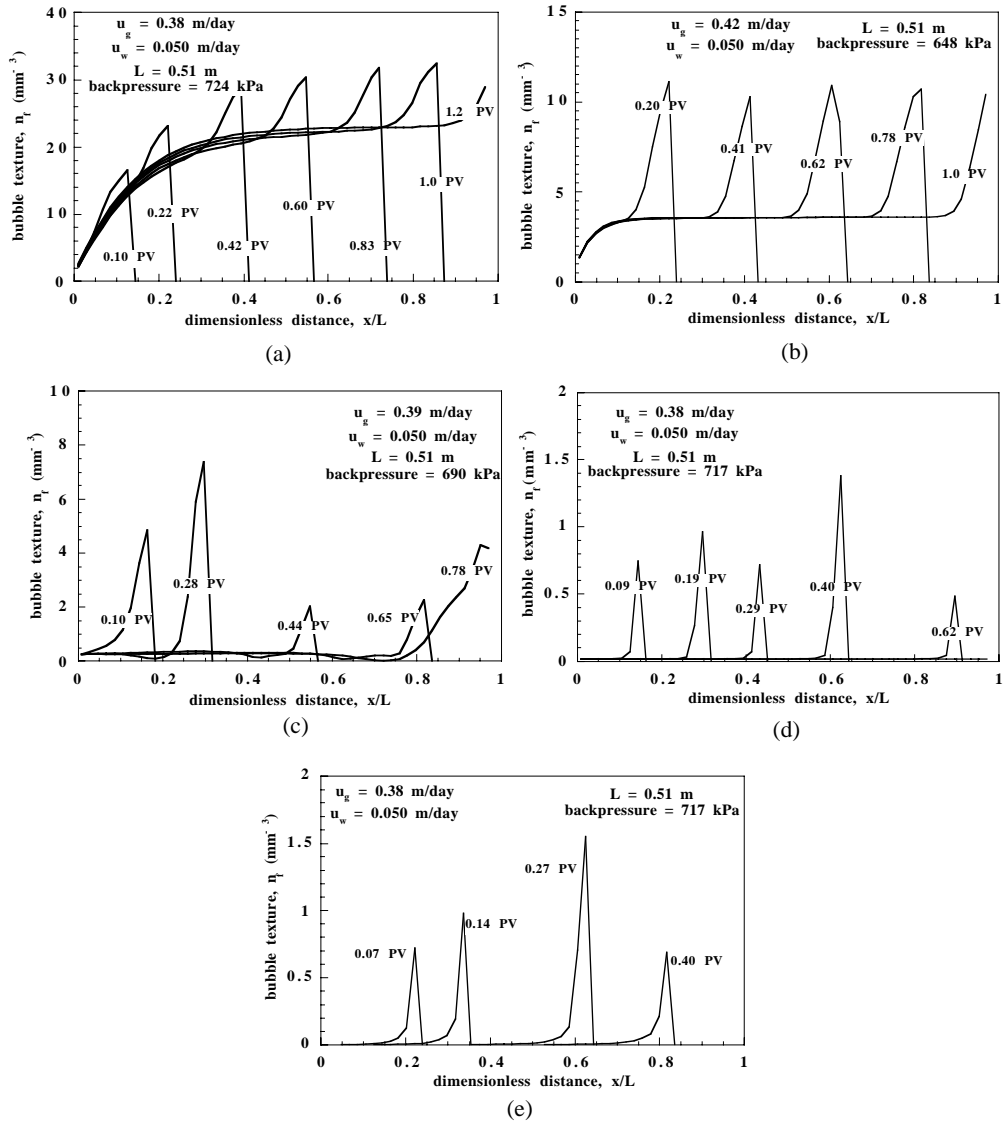


Figure 5. Model transient flowing bubble texture profiles (a) 1 wt% case; (b) 0.1 wt% case; (c) 0.02 wt% case; (d) 0.01 wt% case; (e) 0.005 wt% case.

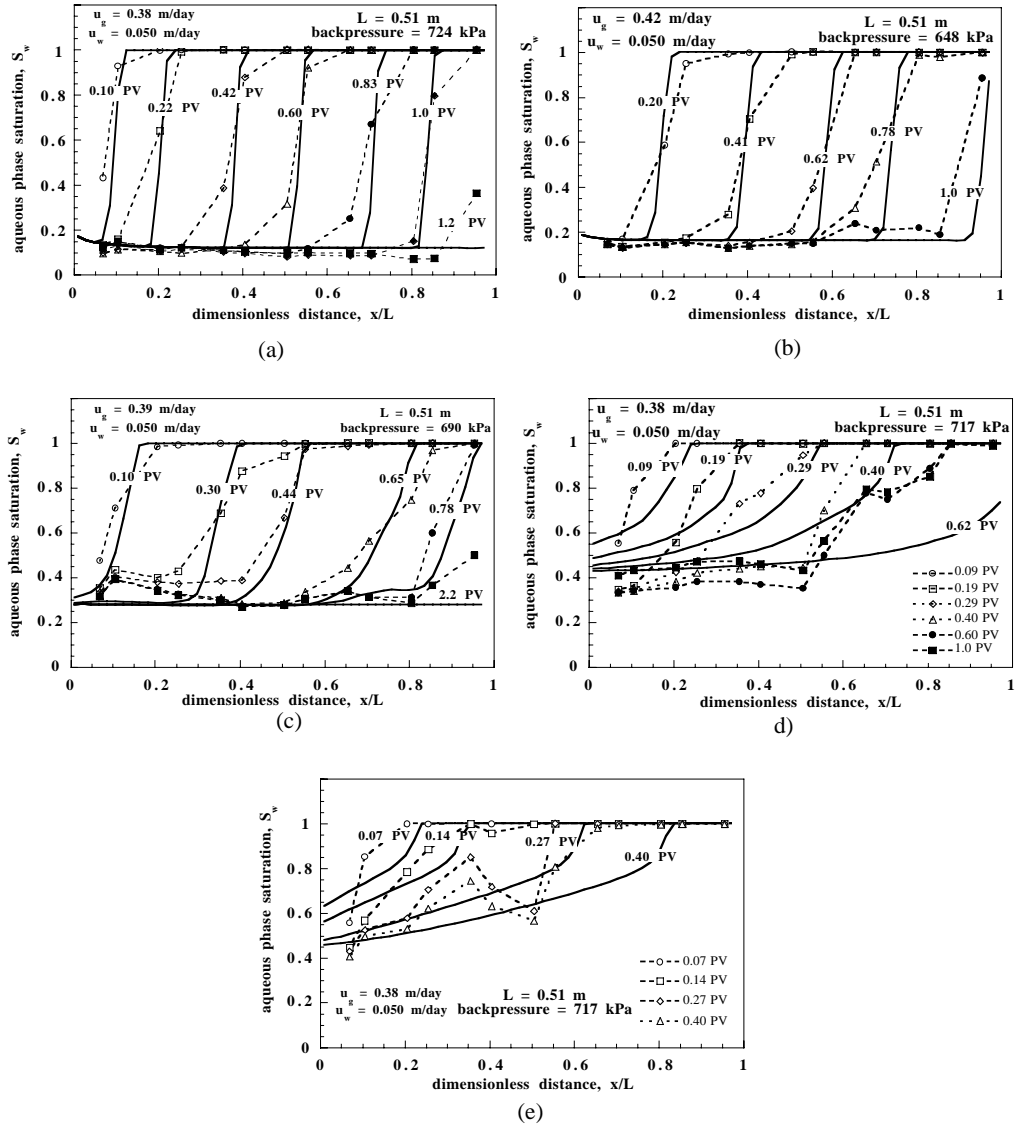
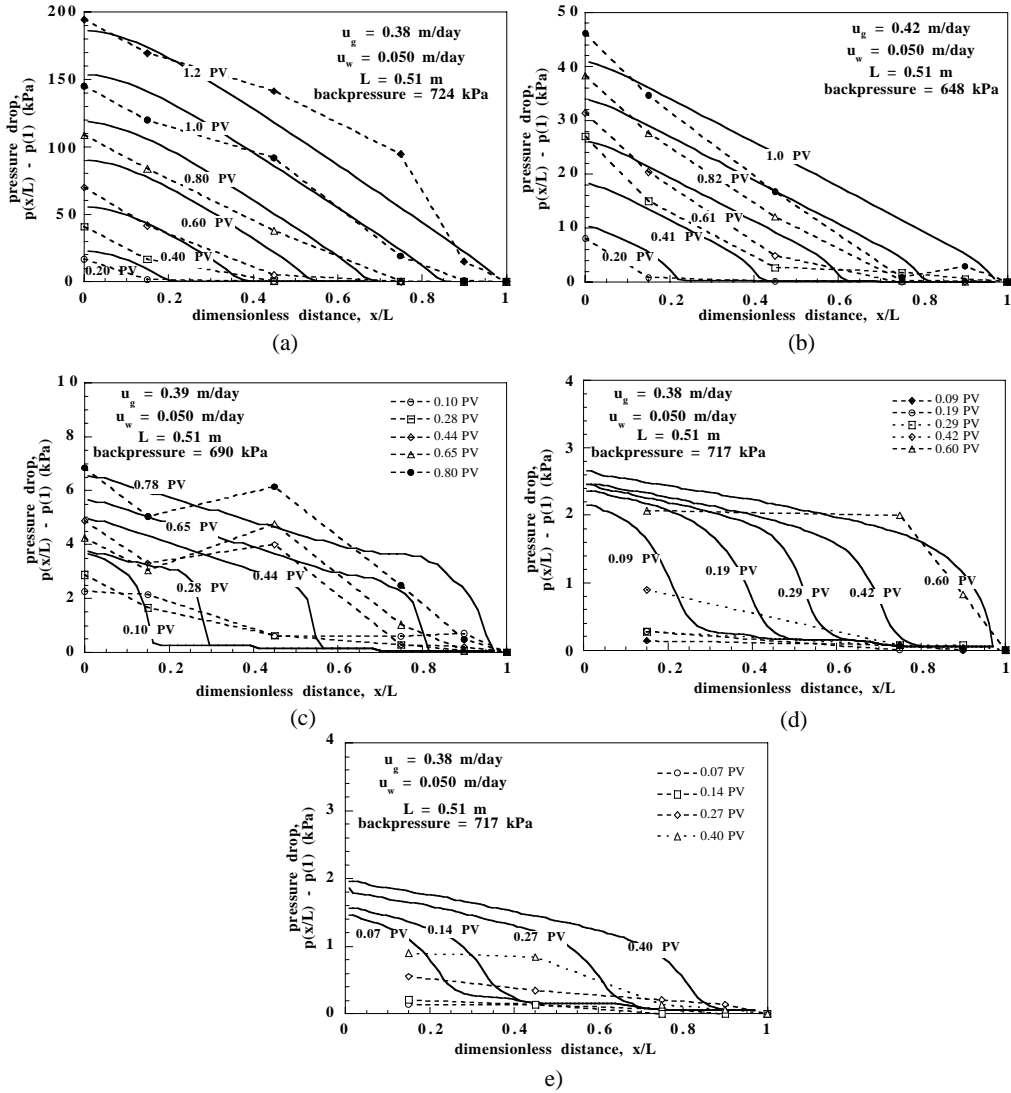


Figure 6. Experimental (symbols connected by dashed lines) and model (solid lines) transient aqueous-phase saturation profiles. (a) 1 wt% case; (b) 0.1 wt% case; (c) 0.02 wt% case; (d) 0.01 wt% case; (e) 0.005 wt% case.



**Figure 7. Experimental (symbols connected by dashed lines) and model (solid lines) transient pressure profiles. (a) 1 wt% case; (b) 0.1 wt% case; (c) 0.02 wt% case; (d) 0.01 wt% case; (e) 0.005 wt% case.**

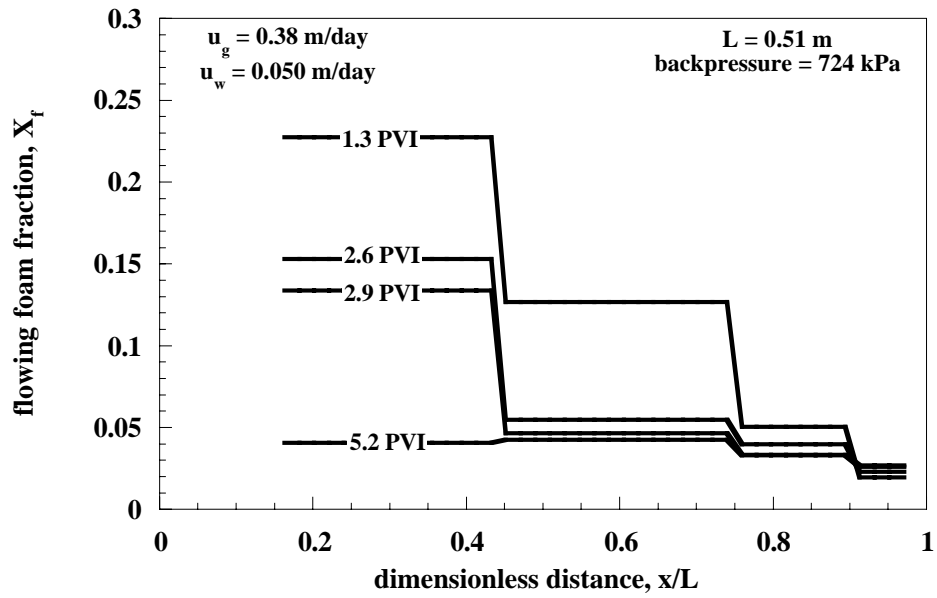


Figure 8. Flowing foam fraction profiles based upon a local equilibrium assumption, 1 wt% case.

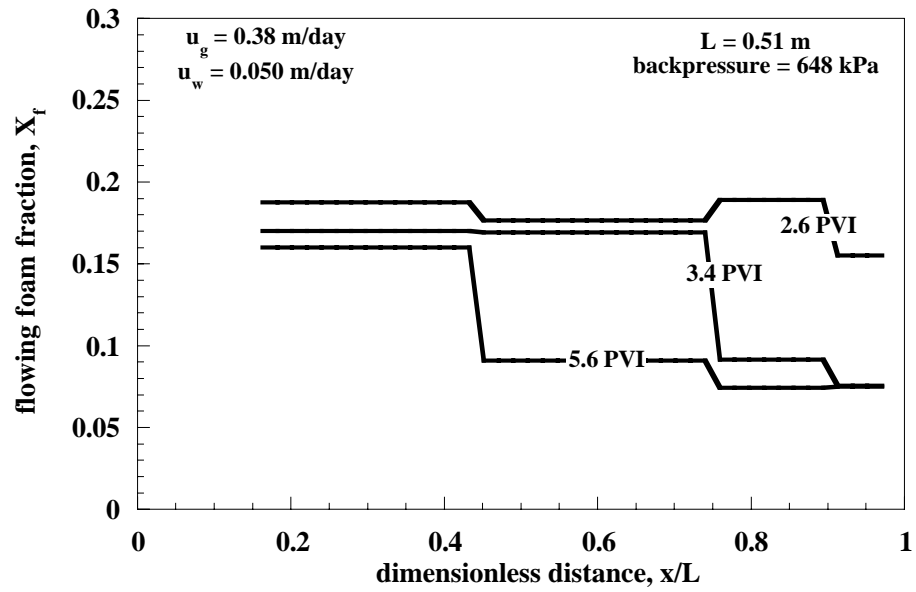


Figure 9. Flowing foam fraction profiles based upon a local equilibrium assumption, 0.1 wt% case.